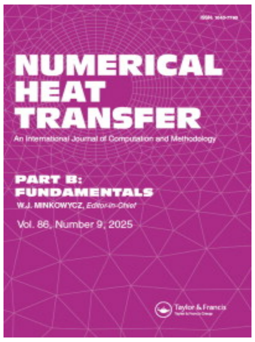

Taylor & Francis
Taylor & Francis Group

Numerical Heat Transfer, Part B: Fundamentals

An International Journal of Computation and Methodology

ISSN: 1040-7790 (Print) 1521-0626 (Online) Journal homepage: www.tandfonline.com/journals/unhb20

Spectral quasi-linearization approach for the swimming of motile microorganisms on the bio-convection Casson nanofluid flow over a rotating circular disk

S. R. Mishra, Titilayo M. Agbaje, Rupa Baithalu & Subhajit Panda

To cite this article: S. R. Mishra, Titilayo M. Agbaje, Rupa Baithalu & Subhajit Panda (2025) Spectral quasi-linearization approach for the swimming of motile microorganisms on the bio-convection Casson nanofluid flow over a rotating circular disk, Numerical Heat Transfer, Part B: Fundamentals, 86:9, 3039-3065, DOI: 10.1080/10407790.2024.2352857

To link to this article: https://doi.org/10.1080/10407790.2024.2352857

NUMERICAL HEAT TRANSFER, PART B: FUNDAMENTALS
2025, VOL. 86, NO. 9, 3039–3065
https://doi.org/10.1080/10407790.2024.2352857

Taylor & Francis
Taylor & Francis Group

Spectral quasi-linearization approach for the swimming of motile microorganisms on the bio-convection Casson nanofluid flow over a rotating circular disk

S. R. Mishra[a], Titilayo M. Agbaje[b], Rupa Baithalu[a], and Subhajit Panda[c]

[a]Department of Mathematics, Siksha 'O' Anusandhan Deemed to be University, Bhubaneswar, Odisha, India; [b]School of Computer Science and Applied Mathematics, University of the Witwatersrand, Johannesburg, South Africa; [c]Centre for Data Science, Siksha 'O' Anusandhan Deemed to be University, Bhubaneswar, Odisha, India

ABSTRACT
The ability of motile microorganisms is used to design of biomedical nanofluidic devices that utilize for targeted drug delivery, to influence heat transfer in nanofluids that are applied to the optimization of cooling system, in biotechnological processes where precise control over fluid flow, etc. However, based upon the several facts, the current investigation lead to propose the heat transfer characteristic of motile microorganisms swimming in a flow of bio-convection nanofluid over a rotating circular disk. The proposed study explores the impacts of dissipative heat generated by the movement of microorganisms, thermal radiation, and chemical reactions. The impact of cross-diffusive property organized by the implementation of Brownian motion and thermophorsis energies the flow phenomena of bio-convection. The set of coupled nonlinear system of non-dimensional equations is obtained by the implementation of similarity rules and further quasi-linearization method is utilized for the solution of this system. The characteristics of diversified parameters are presented through graphs with the variation of the proposed factors within their certain limitations and thee discuss briefly. Further, the important outcomes of the study are presented as; the fluid velocity decelerates due to the enhanced non-Newtonian Casson parameter, whereas the radiating heat for the inclusion of thermal radiation and coupling parameter, that is, Eckert number boosts up the heat transport phenomena.

ARTICLE HISTORY
Received 20 February 2024
Revised 2 April 2024
Accepted 4 May 2024

KEYWORDS
Bio-convection nanofluid; motile microorganism; rotating circular disk; spectral quasi-linearization method; thermal radiation

1. Introduction

Bioconvection in fluids can undergo considerable alteration due to the intricate interplay of thermal transport, particularly affecting thermal transportation. Within a liquid medium, microorganisms or biological entities often aggregate in response to various chemical gradients like light, temperature, or chemical concentrations, a phenomenon termed as bioconvection. This natural process finds extensive application in bioprocessing, where mobile microorganisms play a pivotal role in generating valuable substances such as biofuels, medicines, and food additives. It is important to analyze the swimming behavior of motile microorganisms in biological fluids, in the design of micro-scale medical devices for targeted drug delivery, the ecological implications of microorganism movement in aquatic environments, to the development of nanoscale technologies

CONTACT Subhajit Panda spanda.math@gmail.com Centre for Data Science, Siksha 'O' Anusandhan Deemed to be University, Bhubaneswar, Odisha, India.

such as self-propelled nanorobots for environmental monitoring, improving models and simulations used in various engineering disciplines, including aerospace and mechanical engineering, etc. Their inherent motility facilitates unrestricted movement within the fluid, thereby enhancing the mixing and dispersion of essential substrates such as nutrients without constraint. The primary objectives of the study of Yijie *et al.* [1] include conducting a thorough numerical analysis of the current scenario, focusing on the combined effects of melting transportation and microbial activity on an MHD non-Newtonian nanofluid model. Utilizing the shooting method, numerical assessments of the expressions are executed by employing the MATLAB function bvp4c to facilitate the transformation process. Raut and Mishra [2] explored the varied effects of carbon nanotubes (CNTs) on the stream characteristics of a micro structured polar nanofluid flowing through a permeable surface that expands/contracts, situated within a permeable medium and subject to thermal radiation. Moreover, the standard equations are solved numerically implementing a "fourth-order Runge–Kutta shooting method." The findings indicate that the inclusion of CNTs brings about notable changes in the momentum dynamics and thermal transmission features of the micropolar nanofluid. Arterial diseases, resulting from stenosis, have serious implications. The study by Sahazad *et al.* [3] deliberated the association of nanoparticles on blood stream characteristics, particularly in treating diseases like carotid artery disease and PAD. Furthermore, their work focuses on the flow of SWCNT-MWCNT nanoparticles in a multi-stenotic elliptical artery. Various parameters affecting fluid flow properties are analyzed, along with entropy generation to understand system disorder. Additionally, the temperature profile's physical constraint is investigated using LSA, considering uncertainty through fuzzy environment analysis. Waqas *et al.* [4] introduced a mathematical model aimed at examining the interaction between magnetic fields and the melting process during thermal transport in hybrid nanofluids composed of blood and various nano-sized composites of aluminum alloys over a revolving channel. ODEs are numerically computed using the bvp4c solver, employing the shooting technique within the MATLAB software. Finally, they observed that the radial velocity of fluid diminishes as the magnetic number upsurges, while it improves with the rotational parameter. Shao *et al.* [5] investigated the optimization of thermal transmission rates in a squeezing channel featuring micropolar nanofluid flow, employing advanced statistical concepts. Their study assessed the influence of diverse constraints on heat transfer performance through "*Response Surface Methodology*" (RSM). Additionally, the introduction of dissipative heat resulted from the collaboration between an applied magnetic field and linear radiation was examined in their work. Panda *et al.* [6] considered into the integration of significant conductivity models like the "*Hamilton-Crosser* and *Yamada-Ota models*." The resolution of governing equations involved a collaborative application of the "*Runge-Kutta-Fehlberg*" (RKF) method and the shooting method. Panda *et al.* [7] presented the Williamson fluid flowing through two inclined parallel sheets. Additionally, the significant association of thermal radiation and Ohmic heating are discussed. Moreover, the "*Homotopy perturbation method (HPM)*" is implemented analytically to the finalized transformed equations. Baithalu *et al.* [8], an investigation was carried out on the motion of a magneto polar hybridized nanofluid over an elastic surface. The study emphasized the significance of both shear rate and couple stresses in affecting the stream behavior. The nanoliquid, immersed with Ag and MoS4 nanocomposites in a host liquid of water, was examined to understand their impact on the overall flow characteristics. Their work utilized the "*Response Surface Methodology*" along with "*Analysis of Variance*" to optimize key factors, contributing to a comprehensive analysis of the fluid flow dynamics. Tinker *et al.* [9] anticipated the transient fluid flow of a Casson nanofluid with complete fractional behavior between two parallel plates, considering both slip and no-slip conditions, which was affected by magnetohydrodynamic and Darcian effects. Moreover, a nondimensional fully fractional model is obtained by fractionally transforming the Casson nanofluid model using mixed similarity transformations. Baithalu *et al.* [10] examined the magneto-polar liquid along a widening surface while incorporating chemical reactions and thermal radiation. However, the "*differential transform method*" (DTM) is implanted to solve the proposed model analytically. Before that, similarity conversions are implemented to obtain the transformation to the ordinary system. Baithalu *et al.* [11] investigated over the vertical plate the interaction of nanoparticle shape on the polar hybridized nanofluid flow. Moreover, they utilized a statistical approach called "*Response Surface Methodology*" (RSM) to optimize both skin friction and Nusselt number. Additionally, the standard modeled equations were numerically handled *via* the "*fourth-order Runge-Kutta*" technique based on a shooting method. Pattnaik *et al.* [12] investigate a compelling study on the variation of Fe_3O_4 nanoparticles' shape and its impact on heat transfer, taking into account the influential factor of thermal radiation. Also exploring the nuanced relationship between nanoparticle morphology and thermal radiation's effects. A study showed by Akolade *et al.* [13] described the fluctuating transport characteristics impact the magnetized movement of Casson-Williamson nanoliquids, considering nonlinear thermal radiation effects as they flowing through a sensor plate. Using the "*spectral quasi-linearization method*" (SQLM), all relevant flow parameters were taken into good account. Achraya [14] explored into the thermal behavior of radiative induced nanoliquid stream through a curved, bended interface. The bended surface is wrapped within a round segment with a radius R, supposed to be permeable and constraints of slippery. Additionally, the article thoroughly discusses the permeability features of the interface. Following this, the "*spectral quasi-linearization method*" (SQLM) is established to address the principal nonlinear ODEs. Lawal *et al.* [15] investigated the simultaneous association of variant viscosity, varying thermal conductivity on the transient stream of an Eyring–Powell nanoliquid along an extended sheet. Subsequently, the "*Spectral quasi-linearization method (SQLM)*" was utilized to numerically solve the resulting standard differential equations. Sahoo *et al.* [16] deliberates the entropy generation in the hydrodynamic 2nd-order slip stream of Casson nanoliquid over a horizontal elastic sheet with the mutual association of Hall current and nonlinear thermal radiation. The resulting mathematical model is then solved numerically using the "*spectral quasi-linearization method.*" Bellman and Kalaba [17] introduced "*Haar wavelet-based methods*" for solving boundary value problems with the Haar collocation technique and the "Quasilinearization method" for solving quadratic nonlinearity. Furthermore, a C++ program to implement the wavelet solution approach and perform numerical experiments to validate its effectiveness. The methodology introduced by Motsa [18] revolves around a novel approach that involves linearizing and decoupling the governing equations of systems, subsequently transforming them into a series of subsystems comprised of differential equations. Referred to as the "*spectral local linearization method*," the effectiveness of this method is examined through its application to established boundary layer flow equations. Additionally, the accuracy and stability of the *SLLM* can be enhanced by employing successive overrelaxation techniques. Acharya [19] examined the flow of a hybrid nanofluid comprising MWCNT-Fe_3O_4 particles dispersed in water through a micro-wavy channel. Additionally, the governing equations were solved utilizing the Galerkin-finite-element scheme. Moreover, numerical analysis indicates that altering the amplitude-based wavy texture, whether increasing or decreasing it, enhances flow dynamics and promotes heat transfer more effectively compared to surfaces with a uniform amplitude-based wavy texture. Acharya [20] explored the impacts of the solid–liquid interfacial layer and nanoparticle diameter on the unsteady ferrous-water nanoliquid flow over a spinning disk. However, "Spectral quasilinearization technique" along with the residual error profile is used for solving the governing equations. Again, Acharya [21] presented the interaction between ferrofluid flow and a spinning disk under the influence of a rapidly oscillating magnetic field. Furthermore, the equations generated have been tackled employing a novel "spectral quasi-linearization technique". Acharya [22] investigated revolves around the flow of chemically reactive nanofluid over an inclined spinning disk. Furthermore, the governing equations are solved using SQLM. The results confirm that the normalized thickness parameter increases both radial velocity and nanoparticle concentration. Also, it is clear to see that chemical reaction diminishes the concentration profile under the action of suction but enhances it under injection. Additionally, the fluid temperature decreases under the influence of suction but rises under injection. Acharya [23] explored the hydrothermal dynamics and cooling mechanisms involved in the application of hybrid nanofluid spray onto an inclined revolving disk. After that, those dimensionless equations are solved using the "spectral quasi linearization method (SQLM)." After that, hybrid nanofluid exhibits comparatively higher heat transport as compared to usual nanofluid. The study of Shehzad *et al.* [24] investigates the effect of a horizontal magnetic field on the flow behavior of slippery nanofluids incorporating the Arrhenius activation energy model. Numerical simulations are performed to analyze the fluid flow and heat transfer characteristics under varying magnetic field strengths. Regression analysis techniques are employed to model the relationship between key parameters. Further, Rauf *et al.* [25] presents a numerical investigation of micropolar nanofluid flow between two parallel permeable disks. They have employed thermophysical property variations and the Arrhenius activation energy model. The analysis contributes to understanding the impacts in porous media on the flow phenomena. Hani *et al.* [26] investigates the non-Newtonian Bödewadt nanofluid flow above a stretchable stationary disk using Bayesian and numerical techniques. It explores the heat transfer characteristics on the interplay between non-Newtonian behavior, nanoparticle suspension, and disk flexibility, offering insights into various engineering applications. By employing advanced computational methods, the study contributes to the development of accurate predictive models for such fluid flow scenario. A study conducted by Hayat *et al.* [27] on the magnetohydrodynamic flow of a nanofluid induced by a rotating disk. Furthermore, the analysis includes the consideration of a uniform magnetic field and the application of a velocity slip condition. Rehman *et al.* [28] investigated the flow characteristics of a Casson liquid. The Casson nanoliquid is placed above a solid disk, subject to Navier's slip condition. The resulting differential equations describing the flow are solved using a computational approach. Ahmed *et al.* [29] studied the Casson nanofluid movement over a revolving disk with the association of joule heating as well as microorganism.

1.1. Focus of this research

The focus point of this proposed research work is to analyze the characteristic of diversified factors like dissipative heat, thermal radiation, and chemical reaction on the bio-convection flow of nanofluid for the motile microorganism swimming over a rotating circular disk. This study aims to utilize the spectral quasi-linearization method to analyze a complex nonlinear system under proposed boundary conditions. Specifically, the article focuses on investigating the impact of magnetization on the flow profile across the preamble surface.

1.2. Novelty of the study

The novelty of this study appears due to;

- The inclusion of a mathematical model representing the swimming behavior of motile microorganisms addresses a crucial aspect previously neglected in conventional studies.
- In the current scenario, it is more realistic to investigate the effects of dissipative heat, thermal radiation, and chemical reactions through a rotating disk.
- The comprehensive analysis is obtained by adopting spectral quasi-linearization method with the involved factors with their appropriate range.
- The real-life applications in bio-technology, environmental engineering, and transport system showcasing in a broad sense for the todays research.

2. Mathematical formulation

Let us analyze cylindrical coordinates (r, α, z), that is, indicates an axisymmetric orientation of the object, with $z = 0$. The differential components along the normal direction of flow vanishes due to the flow is symmetric toward the axial direction and the angular velocity formed by the rotational fluid is constant which is far away from the disk surface. Here, V (u, v, w) represents the velocity components toward its usual direction of the coordinate axes respectively. A uniform magnetization of constant strength B_0 is proposed along the normal direction of the flow. Further, T represents fluid temperature, while T_w is constant at the disk surface. The rotational stream that is isolated from the wall the furthest maintains a constant temperature of T_∞. Figure 1 illustrates the geometry of the actual model. The assumption of the rheological properties of the non-Newtonian Casson fluid, that is, the stress tensor components are described as [29]:

$$\tau_{ij} = \begin{Bmatrix} 2\left(\mu_B + \dfrac{P_y}{\sqrt{2\pi}}\right) e_{ij}, \pi > \pi_c \\ 2\left(\mu_B + \dfrac{P_y}{\sqrt{2\pi_c}}\right) e_{ij}, \pi > \pi_c \end{Bmatrix} \tag{1}$$

The shear stress is represented by τ_{ij}, the product of the deformation components is shown by π, the critical value of $\pi = e_{ij}$, e_{ij} is represented by π_c, and the deformation rate component is represented by e_{ij}. Here ρ_y, the yield stress and μ_B, the dynamics velocity relating to of the Casson nanofluid. Conservation laws yield the fundamental transport equations for thermal, solvent energy, steady fluid flow, and bio-convection transports as [29]:

$$\partial_r u + \partial_z w + \frac{u}{r} = 0 \tag{2}$$

$$\begin{aligned} u\partial_r u + w\partial_z w - \frac{v^2}{r} = -\frac{1}{\rho_f}\partial_r p + \upsilon\left(1 + \frac{1}{\beta}\right)\left(\partial_{rr} u + \frac{1}{r}\partial_r u + \partial_{zz} u - \frac{u}{r^2}\right) - \frac{\sigma B_0^2 u}{\rho_f} \\ + \frac{1}{\rho_f}\left[\rho_f \beta^* g(1 - C_\infty)(T - T_\infty) - g(\rho_p - \rho_f)(C - C_\infty) - g\gamma^*(n - n_\infty)(\rho_m - \rho_f)\right] - \frac{\upsilon}{k_p^*} \end{aligned} \tag{3}$$

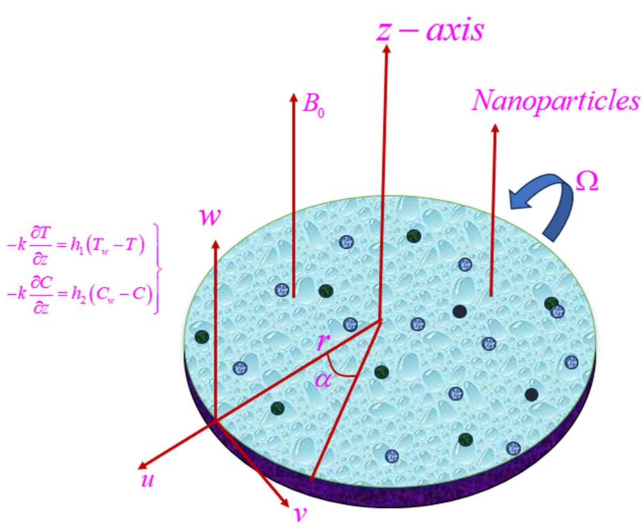

Figure 1. Flow configuration.

$$u\partial_r v + w\partial_z v + \frac{uv}{r} = \upsilon\left(1+\frac{1}{\beta}\right)\left(\partial_{rr}v + \frac{1}{r}\partial_r v + \partial_{zz}v - \frac{v}{r^2}\right) - \frac{\sigma B_0^2 v}{\rho_f} - \frac{\upsilon}{k_p^*}v \tag{4}$$

$$u\partial_r w + w\partial_z w = -\frac{1}{\rho_f}\partial_z p + \upsilon\left(1+\frac{1}{\beta}\right)\left(\partial_{rr}w + \frac{1}{r}\partial_r w + \partial_{zz}w\right) \tag{5}$$

$$\begin{aligned} u\partial_r T + w\partial_z T = \alpha_m\left(\partial_{rr}T + \frac{1}{r}\partial_r T + \partial_{zz}T\right) + \tau\left[D_B(\partial_r C\partial_r T + \partial_z C\partial_z T) + \frac{D_T}{T_\infty}\left((\partial_z T)^2 + (\partial_r C)^2\right)\right] \\ + \frac{\sigma B_0^2}{(\rho Cp)_f}(u^2+v^2) + \frac{1}{(\rho Cp)_f}\partial_z(q_r) \end{aligned} \tag{6}$$

$$u\partial_r C + w\partial_z C = D_B\left(\partial_{rr}C + \frac{1}{r}\partial_r C + \partial_{zz}C\right) + \frac{D_T}{T_\infty}\left(\partial_{rr}T + \frac{1}{r}\partial_r T + \partial_{zz}T\right) - k_c(C - C_\infty) \tag{7}$$

$$u\partial_r n + w\partial_z n + \frac{bW_c}{C_w - C_\infty}\left[\frac{\partial}{\partial z}(n\partial_z C) + \frac{\partial}{\partial r}(n\partial_r C)\right] = D_m\left(\partial_{rr}n + \frac{1}{r}\partial_r n + \partial_{zz}n\right) \tag{8}$$

This illustrates the liquid's electric conductivity (σ), thermal conductivity (k_f), dynamic viscosity (μ), liquid density (ρ_f), Casson parameter (β), and liquid density (υ). Where $\alpha_m = \frac{k_f}{(\rho Cp)_f}$ represents the thermal diffusivity and υ is the kinematic viscosity. The concentration of fluid is denoted by C, while the temperature of the fluid is denoted by T. D_T represents the extent of thermophoresis diffusion, W_c signifies the maximum velocity achievable by a cell in swimming, and D_m denotes the diffusion constant specific to microorganisms. D_B denotes the coefficient related to Brownian diffusion. The following are the boundary conditions [29]:

$$\left.\begin{aligned} &u = w = 0, v = r\Omega, -k\partial_z T = h_1(T_w - T), -k\partial_z C = h_2(C_w - C), \ n = n_w \quad at \ z = 0 \\ &u = v = 0, T = T_\infty, C = C_\infty, n = n_\infty \quad at \quad z \to \infty \end{aligned}\right\} \tag{9}$$

Here, h_1 and h_2 represent the convective coefficients for heat and mass transfer, respectively. Similarly, $T_w, T_\infty, C_w, C_\infty, n_w, n_\infty$ denote the fluid temperature, nanoparticle concentration, and microorganism concentration, respectively, at the surface and away from it. This is achieved by introducing a transformation group [29]:

$$\left.\begin{aligned} &\xi = \sqrt{\frac{2\Omega}{\upsilon}}z, u = \Omega r f'(\xi), v = \Omega r g(\xi), w = -\sqrt{2\Omega\upsilon}f(\xi) \\ &\theta(\xi) = \frac{T - T_\infty}{T_w - T_\infty}, \phi(\xi) = \frac{C - C_\infty}{C_w - C_\infty}, P(\xi) = \frac{p_\infty - p}{\Omega\mu}, \chi(\xi) = \frac{n - n_\infty}{n_w - n_\infty} \end{aligned}\right\} \tag{10}$$

while Eqs. (8–14) take the forms

$$2\left(1+\frac{1}{\beta}\right)f''' + 2ff'' - f'^2 + g^2 - Mf' + \Lambda(\theta - Nr\phi - Nc\chi) - Daf' = 0, \tag{11}$$

$$2\left(1+\frac{1}{\beta}\right)g'' - 2f'g + 2fg' - (M + Da)g = 0, \tag{12}$$

$$(1 + Rd)\theta'' + \Pr\left(Nb\theta'\phi' + Nt\theta'^2\right) + \frac{1}{2}\Pr EcM\left(f'^2 + g^2\right) + \Pr f\theta' = 0, \tag{13}$$

$$\phi'' + \frac{Nt}{Nb}\theta'' + \Pr Lef\phi' - \gamma\phi = 0, \tag{14}$$

$$\chi'' + Lbf\chi' - Pe\left[\phi''(\chi + \delta_1) + \chi'\phi'\right] = 0, \tag{15}$$

With boundary condition (BCs)

$$\left.\begin{array}{l} \left.\begin{array}{c} f'(0) = 0, g(0) = 1, f(0) = 0, \theta'(0) = -\gamma_1(1 - \theta(0)), \\ \phi'(0) = -\gamma_2(1 - \phi(0)), \chi(0) = 1 \end{array}\right) at \quad \xi = 0 \\ f'(\infty) \to 0, g(\infty) \to 0, \theta(\infty) \to 0, \phi(\infty) \to 0, \chi(\infty) = 0 \quad as \quad \xi \to \infty \end{array}\right\} \tag{16}$$

In the equations above, $M = \frac{\sigma B_0^2}{\Omega \rho_f}$ is the magnetic parameter, $Nr = \frac{(\rho_m - \rho_f)(C_w - C_\infty)}{\beta^* \rho_f (1 - C_\infty)(T_w - T_\infty)}$ shows the buoyancy ratio parameter, $Nc = \frac{\gamma(\rho_p - \rho_f)(n_w - n_\infty)}{\beta^* \rho_f (1 - C_\infty)(T_w - T_\infty)}$ is for bio- convection Rayleigh number, $\Lambda = \frac{\beta^* g (1 - C_\infty)(T_w - T_\infty)}{\Omega^2 r}$ is for mixed convection number, $Nb = \frac{\tau D_B (C_w - C_\infty)}{\upsilon}$ (Brownian motion parameter), $\Pr = \frac{\upsilon}{\alpha_m}$ (Prandtl number), $Nt = \frac{\tau D_T (T_w - T_\infty)}{\upsilon T_\infty}$ (thermophoresis parameter), $Le = \frac{\alpha_m}{D_B}$ is the Lewis parameter, $\gamma_1 = \frac{h_1}{k}\sqrt{\frac{\upsilon}{2\Omega}}$ shows Biot number, $\gamma = \frac{k_c \upsilon}{2\Omega}$ Chemical reaction, $Ec = \frac{\upsilon^2}{C_p \Delta T}$ is Eckert number, $Da = \frac{\upsilon}{k_p^* \Omega}$ Darcy number, $\gamma_2 = \frac{h_2}{k}\sqrt{\frac{\upsilon}{2\Omega}}$ Biot number due to concentration, $Lb = \frac{\upsilon}{D_m}$ (Bio-convection Lewis number), $Pe = \frac{bW_c}{D_m}$ (Peclet number),

$$\delta_1 = \frac{n_\infty}{n_w - n_\infty} \text{(Microorganisms difference parameter)}$$

The dimensionless skin frictions (C_f, C_g), Nusselt number (Nu), Sherwood number (Sh), are defined as follows:

$$\mathrm{Re}^{\frac{1}{2}} C_f = \left(1 + \frac{1}{\beta}\right) f''(0), \mathrm{Re}^{\frac{1}{2}} C_g = \left(1 + \frac{1}{\beta}\right) g'(0), \tag{17}$$

$$\mathrm{Re}^{\frac{1}{2}} Nu = -(1 + Rd)\theta'(0), \mathrm{Re}^{\frac{1}{2}} Sh = -\phi'(0), \tag{18}$$

$$\mathrm{Re}^{\frac{1}{2}} Nn = -\chi'(0). \tag{19}$$

Here Re is the local Reynolds number.

3. Numerical simulations

The numerical solution of the ODEs demonstrated in Eqs. (11–15) is obtained by implementing the "*Spectral Quasi-linearisation method (SQLM).*" This method involves linearizing the standard nonlinear equations by implementing the Newton-Raphson based "*quasilinearisation method (QLM),*" which was originally developed by Bellman and Kalaba [17] in 1965. The linearized equations are then resolved by implementing the Chebyshev spectral collocation method. The SQLM is known for its computational accuracy and fast convergence. It utilizes the "*Newton-Raphson method*" to linearize nonlinear ODEs or PDEs. The technique is developed by linearizing the nonlinear components of the standard equations through Taylor series expansion, assuming a small difference among the value of the unknown function at the present iteration level $(m + 1)$ and the value at the previous iteration level (m). For a more detailed explanation of the method, please refer to Motsa [18]. Implanting the SQLM on the set of five nonlinear ODEs, involving five unknown functions $f(\xi), g(\xi), \theta(\xi), \phi(\xi)$, and $\chi(\xi)$ as stated in Eqs. (11–19), results in the following form of equations:

$$a_{0,m} f'''_{m+1} + a_{1,m} f''_{m+1} + a_{2,m} f'_{m+1} + a_{3,m} f_{m+1} + a_{4,m} g_{m+1} + a_{5,m} \theta_{m+1} + a_{6,m} \phi_{m+1} + a_{7,m} \chi_{m+1} = H_1 \tag{20}$$

$$b_{0,m} g''_{m+1} + b_{1,m} g'_{m+1} + b_{2,m} g_{m+1} + b_{3,m} f'_{m+1} + b_{4,m} f_{m+1} = H_2 \tag{21}$$

$$c_{0,m}\theta''_{m+1} + c_{1,m}\theta'_{m+1} + c_{2,m}f'_{m+1} + c_{3,m}f_{m+1} + c_{4,m}g_{m+1} + c_{5,m}\phi'_{m+1} = H_3 \tag{22}$$

$$d_{0,m}\phi''_{m+1} + d_{1,m}\phi'_{m+1} + d_{2,m}\phi_{m+1} + d_{3,m}f_{m+1} + d_{4,m}\theta''_{m+1} = H_4 \tag{23}$$

$$e_{0,m}\chi''_{m+1} + e_{1,m}\chi'_{m+1} + e_{2,m}\chi_{m+1} + e_{3,m}f_{m+1} + e_{4,m}\phi''_{m+1} + e_{5,m}\phi'_{m+1} = H_5 \tag{24}$$

The coefficients $a_{r,m}, b_{r,m}, c_{r,m}, d_{r,m},$ and $e_{r,m}$ (where $r = 1, 2, 3, \ldots$) are already determined from previous calculations and their values are provided by:

$$\begin{aligned}
&a_{0,m} = 2\left(1+\frac{1}{\beta}\right), a_{1,m} = 2f_m, a_{2,m} = -2f'_m - Da - M, a_{3,m} = 2f''_m, a_{4,m} = 2g_m, a_{5,m} = \Lambda,\\
&a_{6,m} = -\Lambda Nr, a_{7,m} = -\Lambda Nc, b_{0,m} = 2\left(1+\frac{1}{\beta}\right), b_{1,m} = 2f_m, b_{2,m} = -2f'_m - Da - M, b_{3,m} = -2g_m,\\
&b_{4,m} = 2g'_m, c_{0,m} = 1 + Rd, c_{1,m} = \Pr\left(Nb\phi'_m + 2Nt\theta'_m + f_m\right), c_{2,m} = \Pr EcMf'_m, c_{3,m} = \Pr\theta'_m,\\
&c_{4,m} = \Pr EcMg_m, c_{5,m} = \Pr Nb\theta'_m, d_{0,m} = 1, d_{1,m} = \Pr Lef_m, d_{2,m} = -\gamma, d_{3,m} = \Pr Le\phi'_m,\\
&d_{4,m} = \frac{Nt}{Nb}, e_{0,m} = 1, e_{1,m} = Lbf_m - Pe\phi'_m, e_{2,m} = -Pe\phi''_m, e_{3,m} = Lb\chi'_m, e_{4,m} = -Pe\chi_m - Pe\delta_1,\\
&e_{5,m} = -Pe\chi'_m
\end{aligned} \tag{25}$$

The right-hand side of Eqs. (20–24) are given as:

$$H_1 = a_{0,m}f'''_m + a_{1,m}f''_m + a_{2,m}f'_m + a_{3,m}f_m + a_{4,m}g_m + a_{5,m}\theta_{m+1} + a_{6,m}\phi_m + a_{7,m}\chi_m - R_f,$$

$$H_2 = b_{0,m}g''_m + b_{1,m}g'_m + b_{2,m}g_m + b_{3,m}f'_m + b_{4,m}f_m - R_g,$$

$$H_3 = c_{0,m}\theta''_m + c_{1,m}\theta'_m + c_{2,m}f'_m + c_{3,m}f_m + c_{4,m}g_m + c_{5,m}\phi'_m - R_\theta,$$

$$H_4 = d_{0,m}\phi''_m + d_{1,m}\phi'_m + d_{2,m}\phi_m + d_{3,m}f_m + d_{4,m}\theta''_m - R_\phi,$$

$$H_5 = e_{0,m}\chi''_m + e_{1,m}\chi'_m + e_{2,m}\chi_m + e_{3,m}f_m + e_{4,m}\phi''_m + e_{5,m}\phi'_m - R_\chi,$$

where

$$\begin{aligned}
&R_f = 2\left(1+\frac{1}{\beta}\right)f'''_m + 2f_mf''_m - {f'_m}^2 + g_m^2 - Mf'_m + \Lambda(\theta_m - Nr\phi_m - Nc\chi_m) - Daf'_m,\\
&R_g = 2\left(1+\frac{1}{\beta}\right)g''_m - 2f'_mg_m + 2f_mg'_m + g_m^2 - (M + Da)g_m\\
&R_\theta = (1 + Rd)\theta''_m + \Pr\left(Nb\theta'_m\phi'_m + Nt{\theta'_m}^2\right) + \frac{1}{2}\Pr EcM\left(f'^2_m + g_m^2\right) + \Pr f_m\theta'_m,\\
&R_\phi = \phi''_m + \frac{Nt}{Nb}\phi''_m + \Pr f_m\phi'_m - \gamma\phi'_m,\\
&R_\chi = \chi''_m + Lbf_m\chi'_m - Pe\left[\phi''_m(\chi_m + \delta_1)\right] + \chi'_m\phi'_m,
\end{aligned} \tag{26}$$

Equations (20–24) constitute the iterative scheme for the spectral quasi-linearisation method, which is subsequently solved using the Chebyshev spectral collocation method. By employing suitable initial approximations, the iteration schemes (20)–(24) are iteratively solved to obtain $f_{m+1}, g_{m+1}, \theta_{m+1}, \phi_{m+1},$ and χ_{m+1} when $m = 1, 2, 3, \ldots$ The initial approximations chosen are given as follows:

$$f_0(\xi) = 0, g_0(\xi) = e^{-\xi}, \theta_0(\xi) = \frac{\gamma_1}{1-\gamma_1}e^{-\xi}, \phi_0(\xi) = \frac{\gamma_2}{1-\gamma_2}e^{-\xi}, \chi_0(\xi) = e^{-\xi} \tag{27}$$

To solve Eqs. (20)–(24), the "*Chebyshev spectral collocation method*" is employed to discretize the equations. This method is applied on the interval $[-1, 1]$ for numerical computations. Prior to applying the spectral method, it is essential to convert the semi-infinite domain of the problem into an approximate truncated domain $[0, L]$ where L is a finite number chosen to be sufficiently large. The transformation $\xi = \frac{L(n+1)}{2}$ is utilized to map the interval $[0, L]$ onto $[-1, 1]$

In addition, a differentiation matrix D is introduced, which is used to evaluate the derivatives of the unknown variables $f(\xi), g(\xi), \theta(\xi), \phi(\xi),$ and $\chi(\xi)$ at the collocation points. This estimation is achieved through a matrix-vector product given as:

$$\left.\begin{array}{ll} \frac{df}{d\xi} = \sum_{p=0}^{Nx} D_{pq} f(\eta_p) = DF, \ \ q = 0, 1, 2, \ldots N_x, & \frac{dg}{d\xi} = \sum_{p=0}^{Nx} D_{pq} g(\eta_p) = DG, \ \ q = 0, 1, 2, \ldots N_x \\ \frac{d\theta}{d\xi} = \sum_{p=0}^{Nx} D_{pq} \theta(\eta_p) = D\Theta, \ \ q = 0, 1, 2, \ldots N_x, & \frac{d\phi}{d\xi} = \sum_{p=0}^{Nx} D_{pq} \phi(\eta_p) = D\Phi, \ \ q = 0, 1, 2, \ldots N_x, \\ \frac{d\chi}{d\xi} = \sum_{p=0}^{Nx} D_{pq} \chi(\eta_p) = DX, \ \ q = 0, 1, 2, \ldots N_x & \end{array}\right\} \tag{28}$$

Here $N_x,$ is the number of collocation points, $D = \frac{2D}{L}$ and

$$\begin{array}{ll} F = [f(\eta_0), f(\eta_1), \ldots, f(\eta_{N_x})]^T, & G = [g(\eta_0), g(\eta_1), \ldots, g(\eta_{N_x})]^T, \\ \Theta = [\theta(\eta_0), \theta(\eta_1), \ldots, \theta(\eta_{N_x})]^T, & \Phi = [\phi(\eta_0), \phi(\eta_1), \ldots, \phi(\eta_{N_x})]^T \\ \chi = [\chi(\eta_0), \chi(\eta_1), \ldots, \chi(\eta_{N_x})]^T. & \end{array}$$

In matrix notation, the SQLM approach for Eqs. (20)–(24) can be succinctly expressed as:

$$\begin{bmatrix} A_{11} & A_{12} & A_{13} & A_{14} & A_{15} \\ A_{21} & A_{22} & A_{23} & A_{24} & A_{25} \\ A_{31} & A_{32} & A_{33} & A_{34} & A_{35} \\ A_{41} & A_{42} & A_{43} & A_{44} & A_{45} \\ A_{51} & A_{52} & A_{53} & A_{54} & A_{55} \end{bmatrix} \begin{bmatrix} f_{m+1} \\ g_{m+1} \\ \theta_{m+1} \\ \phi_{m+1} \\ \chi_{m+1} \end{bmatrix} = \begin{bmatrix} H_1 \\ H_2 \\ H_3 \\ H_4 \\ H_5 \end{bmatrix}, \tag{29}$$

where

$$\begin{array}{l} A_{11} = a_{0,m}D^3 + diag[a_{1,m}]D^2 + diag[a_{2,m}]D + diag[a_{3,m}], A_{12} = diag[a_{4,m}], A_{13} = a_{5,m}I, \\ A_{14} = a_{6,m}I, A_{15} = a_{7,m}I, \\ A_{21} = diag[b_{3,m}]D + diag[a_{4,m}], A_{22} = b_{0,m}D^2 + diag[b_{1,m}]D + diag[a_{4,m}], A_{23} = 0, A_{24} = 0, \\ A_{25} = 0, \\ A_{31} = diag[c_{2,m}]D + diag[c_{3,m}], A_{32} = diag[c_{4,m}], A_{32} = c_{0,m}D^2 + diag[c_{1,m}]D, \\ A_{34} = diag[c_{5,m}]D, A_{34} = 0, A_{35} = 0, \\ A_{41} = diag[d_{3,m}], A_{42} = 0, A_{43} = 0, A_{44} = d_{0,m}D^2 + diag[d_{1,m}]D + , d_{2,m}I, A_{45} = d_{4,m}D^2, \\ A_{51} = diag[e_{3,m}], A_{52} = 0, A_{53} = 0, A_{54} = diag[e_{4,m}]D^2 + diag[e_{5,m}]D, \\ A_{55} = e_{0,m}D^2 + diag[e_{1,m}]D + diag[e_{2,m}]. \end{array}$$

In the above representation, the symbol "*diag*" represents a diagonal matrix with dimensions $(N_x + 1) \times (N_x + 1),$ and I denotes an identity matrix of size $(N_x + 1) \times (N_x + 1),$ and D signifies differentiation with respect to ξ.

4. Results and discussion

In this study, we have employed the Spectral quasi-linearisation method to solve the fluid model under consideration. The obtained results were compared with previously published literature to validate the findings of our study. In order to exhibit the convergence of SQLM, we have considered the solution errors, which represent the disparities between the estimated function values at successive iterations. To depict the convergence of SQLM, we have employed infinity norms, which are characterized as follows:

$$E_f = \max_{0\le j\le N_x} \|f_{m+1,j} - f_{m,j}\|_\infty, \quad E_g = \max_{0\le j\le N_x} \|g_{m+1,j} - g_{m,j}\|_\infty,$$
$$E_\theta = \max_{0\le j\le N_x} \|\theta_{m+1,j} - \theta_{m,j}\|_\infty, \quad E_\phi = \max_{0\le j\le N_x} \|\phi_{m+1,j} - \phi_{m,j}\|_\infty,$$
$$E_\chi = \max_{0\le j\le N_x} \|\chi_{m+1,j} - \chi_{m,j}\|_\infty,$$

To further validate the accuracy of the SQLM, we assess the infinity norm of the residual error for each function. This verification process entails substituting the approximate solutions into the differential equations (11)–(15). The norms are defined as follows:

$$\|\mathrm{Re}\,s(f)\|_\infty = \|2\left(1+\frac{1}{\beta}\right)f_m''' + 2f_m f_m'' - f_m'^{\,2} + g_m^2 - Mf_m' + \Lambda(\theta_m - Nr\phi_m - Nc\chi_m) - Daf_m'\|_\infty,$$

$$\|\mathrm{Re}\,s(g)\|_\infty = \|2\left(1+\frac{1}{\beta}\right)g_m'' - 2f_m' g_m + 2f_m g_m' + g_m^2 - (M + Da)g_m\|_\infty$$

$$\|\mathrm{Re}\,s(\theta)\|_\infty = \|(1+Rd)\theta''_m + \Pr\left(Nb\theta'_m\phi'_m + Nt\theta'^{\,2}_m\right) + \frac{1}{2}\Pr EcM\left(f'^2_m + g_m^2\right) + \Pr f_m\theta'_m\|_\infty$$

$$\|\mathrm{Re}\,s(\phi)\|_\infty = \|\phi''_m + \frac{Nt}{Nb}\phi''_m + \Pr f_m\phi'_m - \gamma\phi'_m\|_\infty,$$

$$\|\mathrm{Re}\,s(\chi)\|_\infty = \|\chi_m'' + Lbf_m\chi_m' - Pe\left[\phi_m''(\chi_m + \delta_1)\right] + \chi_m'\phi'_m\|_\infty,$$

The solution errors $(E_f, E_g, E_\theta, E_\phi, E_\chi)$ obtained using the SQLM at various iteration levels are demonstrated in Table 1. It is worth observing that the error norms for each function consistently diminishing as the number of iterations increases. This consistent decrease in error norms highlights the rapid convergence of the SQLM, as the errors progressively diminish with each iteration step.

Table 2 depicts the relationship between the number of iterations and the variation in residual errors. The data clearly indicates that as the number of iterations increases, the residual error consistently decreases. This decline in the residual norm indicates an enhancement in the accuracy of the approximate solutions produced by the SQLM as more iteration are conducted. The evident convergence, characterized by the decreasing residual norms, emphasizes the SQLM's effectiveness as a reliable and accurate numerical method for addressing nonlinear differential equations.

Further, structural presentation for each of the pertinent factors involved in the flow phenomena is depicted graphically. The computation is deployed in a statistical manner exhibiting these

Table 1. Convergence of $f(\xi), g(\xi), \theta(\xi), \phi(\xi),$ and $\chi(\xi)$.

Iterations	E_f	E_g	E_θ	E_ϕ	E_χ
1	$1.510\times10^{(-2)}$	$1.190\times10^{(-1)}$	$1.231\times10^{(-1)}$	$8.730\times10^{(-4)}$	$4.704\times10^{(-1)}$
2	$8.689\times10^{(-3)}$	$1.302\times10^{(-3)}$	$8.800\times10^{(-4)}$	$6.594\times10^{(-5)}$	$3.297\times10^{(-3)}$
3	$1.788\times10^{(-5)}$	$3.505\times10^{(-6)}$	$2.904\times10^{(-6)}$	$4.624\times10^{(-7)}$	$1.576\times10^{(-5)}$
4	$1.696\times10^{(-9)}$	$2.002\times10^{(-10)}$	$7.953\times10^{(-10)}$	$3.870\times10^{(-12)}$	$7.487\times10^{(-10)}$
5	$5.866\times10^{(-10)}$	$1.534\times10^{(-11)}$	$9.349\times10^{(-10)}$	$1.062\times10^{(-12)}$	$1.294\times10^{(-10)}$
6	$1.469\times10^{(-10)}$	$5.601\times10^{(-11)}$	$2.071\times10^{(-10)}$	$8.250\times10^{(-13)}$	$4.176\times10^{(-11)}$
7	$4.650\times10^{(-11)}$	$6.242\times10^{(-11)}$	$1.736\times10^{(-10)}$	$1.108\times10^{(-13)}$	$2.385\times10^{(-11)}$
8	$4.819\times10^{(-11)}$	$8.366\times10^{(-11)}$	$2.158\times10^{(-10)}$	$2.567\times10^{(-13)}$	$2.278\times10^{(-11)}$
9	$2.602\times10^{(-11)}$	$8.570\times10^{(-11)}$	$1.106\times10^{(-10)}$	$1.503\times10^{(-13)}$	$2.356\times10^{(-11)}$
10	$3.493\times10^{(-11)}$	$4.178\times10^{(-11)}$	$1.127\times10^{(-10)}$	$8.953\times10^{(-13)}$	$8.652\times10^{(-10)}$

Table 2. Residual error for Eqs. (11)–(15).

Iterations	$\|\mathrm{Re}\,s(f)\|_\infty$	$\|\mathrm{Re}\,s(g)\|_\infty$	$\|\mathrm{Re}\,s(\theta)\|_\infty$	$\|\mathrm{Re}\,s(\phi)\|_\infty$	$\|\mathrm{Re}\,s(\chi)\|_\infty$
1	$1.462\times10^{(-2)}$	$5.469\times10^{(-4)}$	$2.256\times10^{(-3)}$	$6.572\times10^{(-6)}$	$2.392\times10^{(-3)}$
2	$1.898\times10^{(-5)}$	$3.248\times10^{(-6)}$	$7.144\times10^{(-6)}$	$3.831\times10^{(-7)}$	$1.675\times10^{(-5)}$
3	$3.232\times10^{(-10)}$	$8.577\times10^{(-11)}$	$3.162\times10^{(-10)}$	$2.258\times10^{(-11)}$	$6.097\times10^{(-10)}$
4	$1.421\times10^{(-10)}$	$4.822\times10^{(-11)}$	$2.227\times10^{(-10)}$	$5.447\times10^{(-12)}$	$2.757\times10^{(-10)}$
5	$2.347\times10^{(-11)}$	$6.328\times10^{(-11)}$	$3.964\times10^{(-10)}$	$4.549\times10^{(-12)}$	$2.509\times10^{(-10)}$
6	$1.084\times10^{(-11)}$	$3.812\times10^{(-11)}$	$2.708\times10^{(-10)}$	$5.554\times10^{(-12)}$	$3.011\times10^{(-10)}$
7	$6.108\times10^{(-11)}$	$4.002\times10^{(-11)}$	$2.655\times10^{(-10)}$	$5.531\times10^{(-12)}$	$3.584\times10^{(-10)}$
8	$3.250\times10^{(-11)}$	$4.494\times10^{(-11)}$	$1.986\times10^{(-10)}$	$4.270\times10^{(-12)}$	$4.084\times10^{(-10)}$
9	$3.131\times10^{(-11)}$	$4.589\times10^{(-11)}$	$2.700\times10^{(-10)}$	$4.370\times10^{(-12)}$	$2.625\times10^{(-10)}$
10	$3.310\times10^{(-11)}$	$3.868\times10^{(-11)}$	$1.840\times10^{(-10)}$	$4.936\times10^{(-12)}$	$2.795\times10^{(-10)}$

Table 3. Comparison in limiting cases of the values of $-\theta'(0)$ with previously published work of Ref. [27] and Ref. [28], for different values of $M, Le, \Pr, Nb, Nt$.

M	Le	Pr	Nb	Nt	Ref. [27]	Ref. [28]	Present
0.0	0.8	1.0	0.3	0.2	0.30494	0.30500	0.3049
0.7					0.24421	0.2443	0.2442
1.4					0.17566	0.1757	0.1757
0.3	0.8	1.0	0.3	0.2	0.32655	0.3266	0.3265
					0.30360	0.3036	0.3036
					0.28715	0.2872	0.2871
0.3	0.5	1.0	0.3	0.2	0.29633	0.2964	0.2963
	1.0				0.28954	0.2896	0.2895
	1.5				0.28395	0.2839	0.2839
0.3	0.8	0.5	0.3	0.2	0.24989	0.2499	0.2499
		1.0			0.29211	0.2922	0.2921
		1.5			0.32286	0.3229	0.3229
0.3	0.8	1.0	0.5	0.2	0.26341	0.2635	0.2634
			0.7		0.23677	0.2368	0.2367
			1.0		0.20056	0.2006	0.2006
0.3	0.8	1.0	0.3	0.5	0.25913	0.2591	0.2591
				0.7	0.23865	0.2387	0.2386
				1.0	0.21010	0.2102	0.2101

Table 4. Comparison in limiting cases of the values of $-\phi'(0)$, with previously published work of Ref. [27] and Ref. [28], for different values of $M, Le, \Pr, Nb, Nt$.

M	Le	Pr	Nb	Nt	Ref. [27]	Ref. [28]	Present
0.0	0.8	1.0	0.3	0.2	0.27000	0.2701	0.2700
0.7					0.25387	0.2539	0.2539
1.4					0.23722	0.2373	0.2372
0.3	0.8	1.0	0.3	0.2	0.27583	0.2759	0.2758
					0.26933	0.2694	0.2693
					0.26493	0.2649	0.2649
0.3	0.5	1.0	0.3	0.2	0.21373	0.2138	0.2137
	1.0				0.30132	0.3014	0.3013
	1.5				0.38690	0.3869	0.3869
0.3	0.8	0.5	0.3	0.2	0.22934	0.2294	0.2293
		1.0			0.26624	0.2663	0.2662
		1.5			0.31262	0.3127	0.3127
0.3	0.8	1.0	0.5	0.2	0.30338	0.3034	0.3034
			0.7		0.31875	0.3188	0.3187
			1.0		0.32959	0.3297	0.3296
0.3	0.8	1.0	0.3	0.5	0.22206	0.2221	0.2221
				0.7	0.22539	0.2256	0.2254
				1.0	0.22855	0.2228	0.2286

factors considering within the particular range. The important fact is that the numerical results are utilized for the validation of the current outcomes with that of the novel work of Hayat *et al.* [27] and Rehman *et al.* [28] for the various values of the parameters. These results for the heat transfer rate $-(\theta'(0))$ are depicted in Table 3 which coincides with the earlier result in a good tolerance limit by considering a few significant digits. These unique results are also validating the fact from the computation of the residual error. Moreover, the results of Sherwood number for

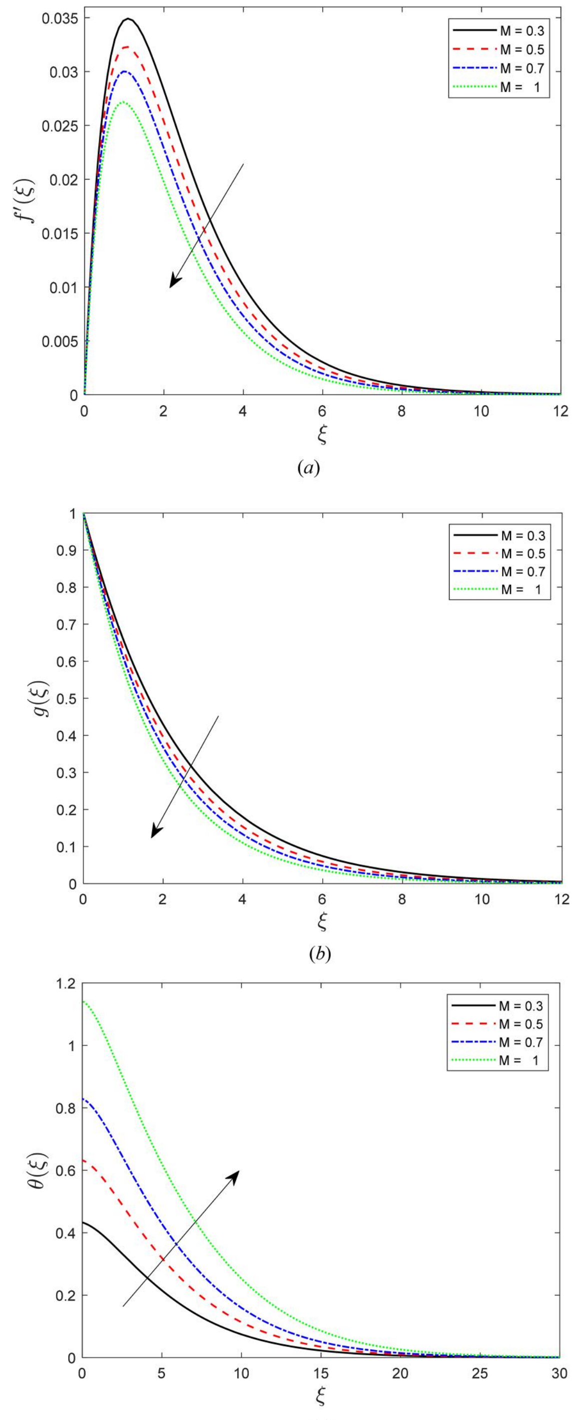

Figure 2. (*a*) Graphical illustration of *M* on $f(\xi)$. (*b*) Graphical illustration of *M* on $g(\xi)$. (*c*) Graphical illustration of *M* on $\theta(\xi)$.

the diversified factors are exhibited in Table 4 and compared with the outcomes of Hayat *et al.* [27] and Rehman *et al.* [28]. It is seen that, the current outcomes validate with these earlier studies in a good correlation representing the convergence analysis of the proposed methodology.

4.1. Variation of magnetic parameter

The flow phenomenon of bio-convection Casson nanofluid flowing on a rotating disk is imposed with transverse magnetic field along the normal direction shows the impact of magnetization. The parametric analysis for the magnetic effect is depicted for the consideration of the numerical values of M within the range of $0.3 \leq M \leq 1$. Figure 2*a* portrays the analysis of the strength of the magnetic constraint on the momentum distribution. The introduction of a magnetized field into the flow induces a resistive force, generating the "Lorentz force" which opposes fluid motion. Consequently, it is noteworthy that increasing magnetization slows down the flow profile across the entire flow domain. One of the interesting facts rendered is that, near to the surface a sudden hike in the profile is exhibited and afterward the fall is also sharp to meet adequate boundary conditions. The deceleration in the surface thickness is manifesting its utility in various production processes in industries to avoid maximum damages. Figure 2*b* depicts the transverse momentum profile for the diversified values of the magnetic parameter. The result reveals that for the lower values of the magnetic strength the fluid velocity exhibits its maximum strength within the domain at all points however, increasing magnetization attenuates the profile asymptotically. Further, Figure 2*c* contributes the role of magnetic properties on the fluid temperature profile for the bio-convective Casson nanofluid. The magnetic field strength diminishes the fluid velocity due to the density of solute particles within the fluid. It becomes apparent that particles deposited on the surface accumulate energy, subsequently leading to their growth and consequent enhancement of the fluid's temperature profile. This hike in the profile is useful in cooling of the base/surface.

4.2. Behavior of Casson parameter

The bio-convection nanofluid shows its non-Newtonian characteristic due to the introduction of the non-Newtonian Casson parameter. Figures 3*a*, *b* shows the behavior of Casson parameter which plays a crucial role on the axial and transverse velocity profile of bio-convection Casson nanofluid. To present is behavior, the numerical value of the Casson parameter β is restricted to the range of $0.5 \leq \beta \leq 2$. However, the higher value of the parameter β leads to the case of Newtonian fluid. This model describes non-Newtonian fluids with yield stress and its impact on the flow phenomena. In mathematical terms, as the Casson parameter increases, the prominence of the yield stress intensifies. Furthermore, a higher Casson parameter value correlates with an increase in flow resistance, consequently reducing the axial velocity. In a broader sense, there exists a threshold for the initiation of fluid movement due to yield stress, with higher Casson parameter values imposing greater restrictions on fluid flow. Further, enhanced Cason parameter also favors in retarding the transverse momentum profile significantly.

4.3. Beavior of porosity parameter

The bio-convection stream of Casson nanofluid is also affected by the inclusion of porosity on the fluid medium. Figures 4*a*, *b* presents the description of the permeability parameter on the axial as well as transverse velocity distribution. The physical description is obtain for the variation of the parameter Da within the standard numerical value as $0 \leq Da \leq 1.5$. The assigned $Da = 0$ indicates the flow through nonporous medium and further the no-zero values deal with the variation of the parameter where the fluid past a porous medium. The observation reveals that the

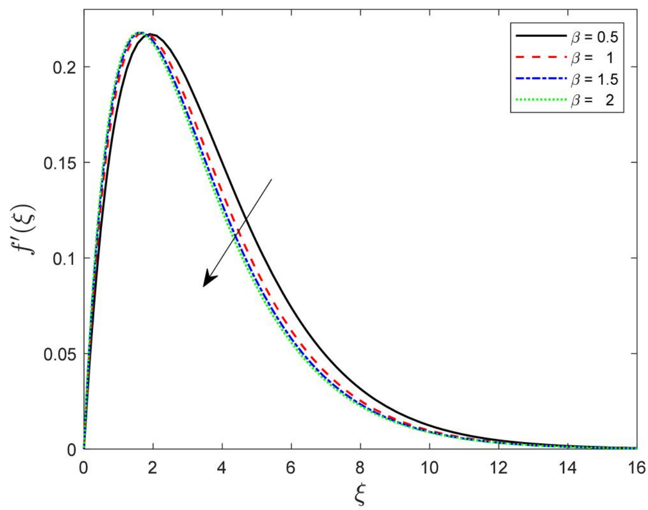

(*a*)

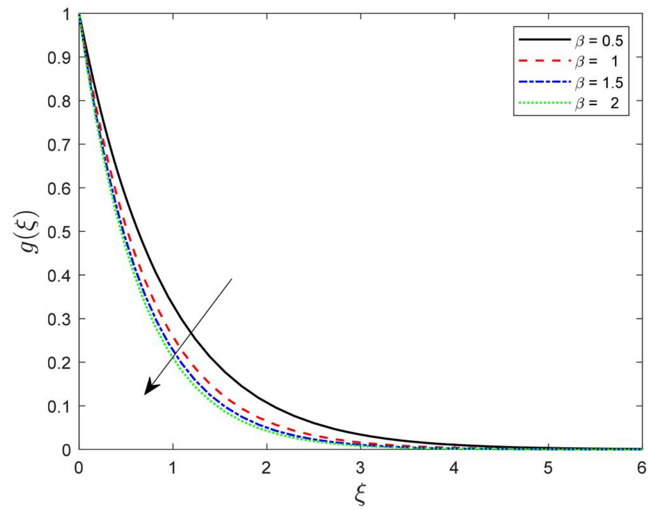

(*b*)

Figure 3. (*a*) Graphical illustration of β on $f^{'}(\xi)$. (*b*) Graphical illustration of β on $g(\xi)$.

increasing porosity put a greater strength for which the fluid velocity supposed to reduce its strength drastically. This is because porosity act as a resistance to the axial motion of the fluid leading to retard the axial velocity. Further, the transverse velocity distribution also affected by the increasing porosity and therefore, the fluid velocity in the transverse direction asymptotically.

4.4. Behavior of thermal Biot number

The proposed boundary condition of the temperature profile depends upon the convective condition due to heat transfer which produces the influence of thermal Biot number. Figures 5*a*, *b* depicts the impact of thermal Biot number and its characteristic on the transverse velocity distribution and the temperature distribution, respectively. The variation presented within the numerical range of $0.1 \leq \gamma_1 \leq 0.7$. The dimensionless parameter γ_1 is described as the ratio of resistance due to heat transmission inside the solid body to the resistance at the fluid-surface

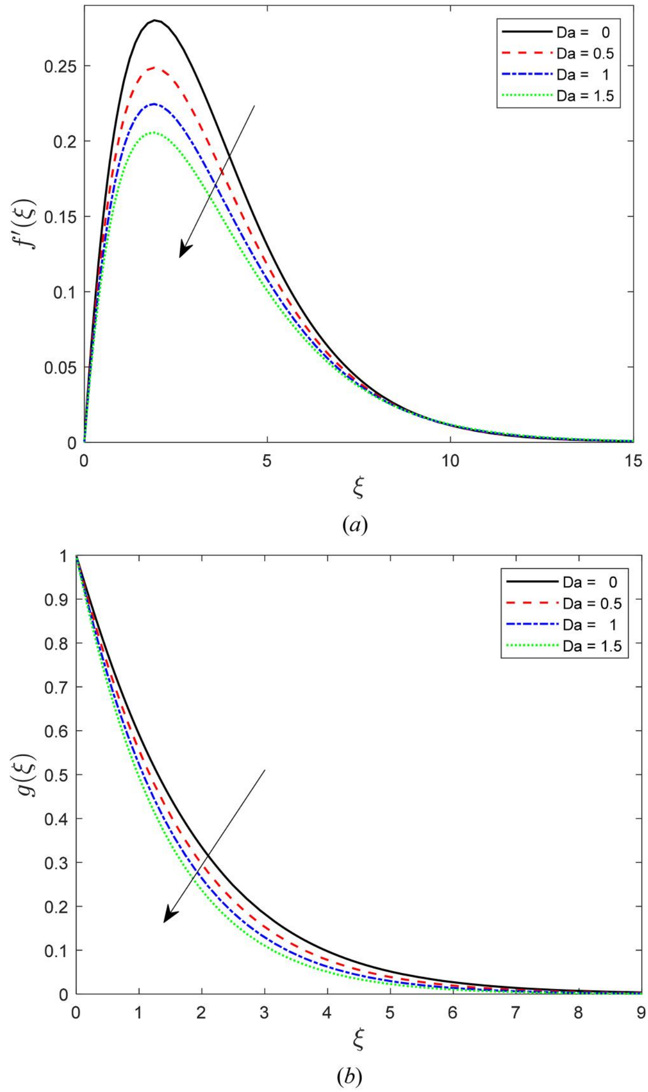

Figure 4. (*a*) Graphical illustration of Da on $f'(\xi)$. (*b*) Graphical illustration of Da on $g(\xi)$.

interface. As the Biot number increases, it signifies slower heat conduction at the solid surface interface for which it lead to absorbed more energy toward the interface layer. Therefore, the fluid temperature reduces significantly with increasing Biot number. Further, a more significant influence of the solid phase occurs with increasing thermal Biot number for which the overall temperature increases significantly within the Casson nanofluid. Moreover, the elevated γ_1 lead to rapid establishment of the thermal equilibrium between the solid and fluid phases influence the temperature distribution.

4.5. Variation of bio-convection Rayleigh number

The bio-convection Rayleigh number has important aspects for the influence of velocity distribution which is obtained due to the interaction of buoyancy-driven forces on the velocity distribution. Figures 6*a*, *b* demonstrates the variation of bio-convection Rayleigh number on the axial as well as transverse velocity distribution respectively. The description is presented for the variation

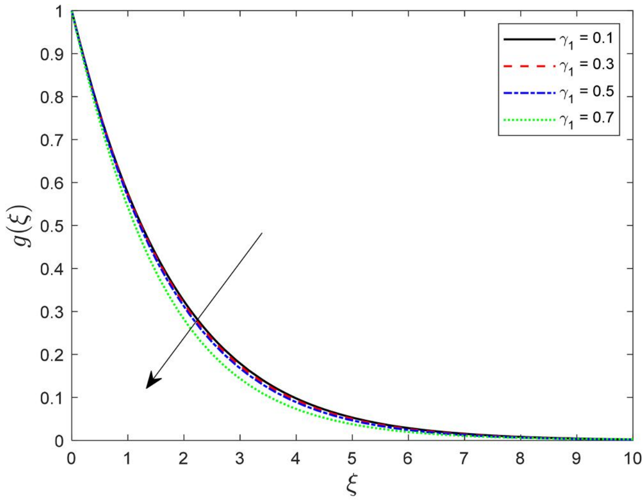

(*a*)

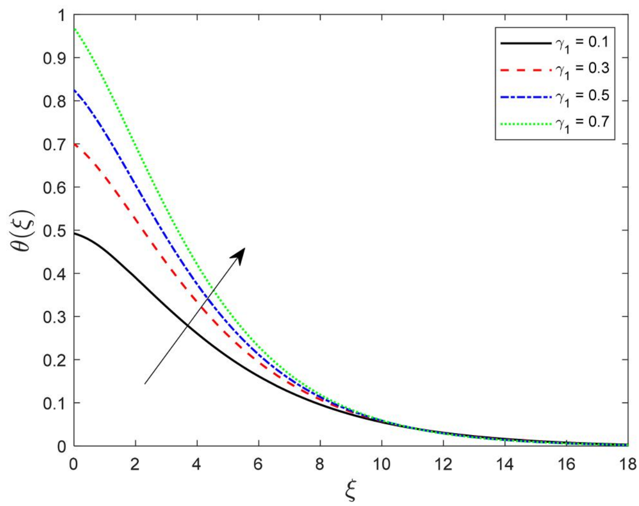

(*b*)

Figure 5. (*a*) Graphical illustration of γ_1 on $g(\xi)$. (*b*) Graphical illustration of γ_1 on $\theta(\xi)$.

of the parameter Nc, within the range $0.1 \leq Nc \leq 0.7$. A rise in the bio-convection Rayleigh number exerts greater influence than buoyancy force, leading to a notable deceleration in the axial velocity distribution. Moreover, higher Rayleigh numbers notably amplify the secondary velocity, resulting in the expansion of the transverse velocity distribution of the Casson fluid.

4.6. Variation of Brownian motion

Brownian motion denotes to the random motion of the particle due to their collisions with the surrounding fluid molecules. The appearance of the Brownian motion is because of the cross-diffusion among the solutal and heat fluxes. Figures 7*a*, *b* corresponds to the variation of the Brownian motion on the concentration vis-à-vis the temperature distribution of the nanofluid. The description is presented briefly for the numeric range of Nb as $0.1 \leq Nb \leq 0.9$. The increasing dispersion and mixing of the nanoparticle in the nanofluid are due to the Brownian motion. These phenomena lead to decelerate the concentration profile significantly. Brownian motion

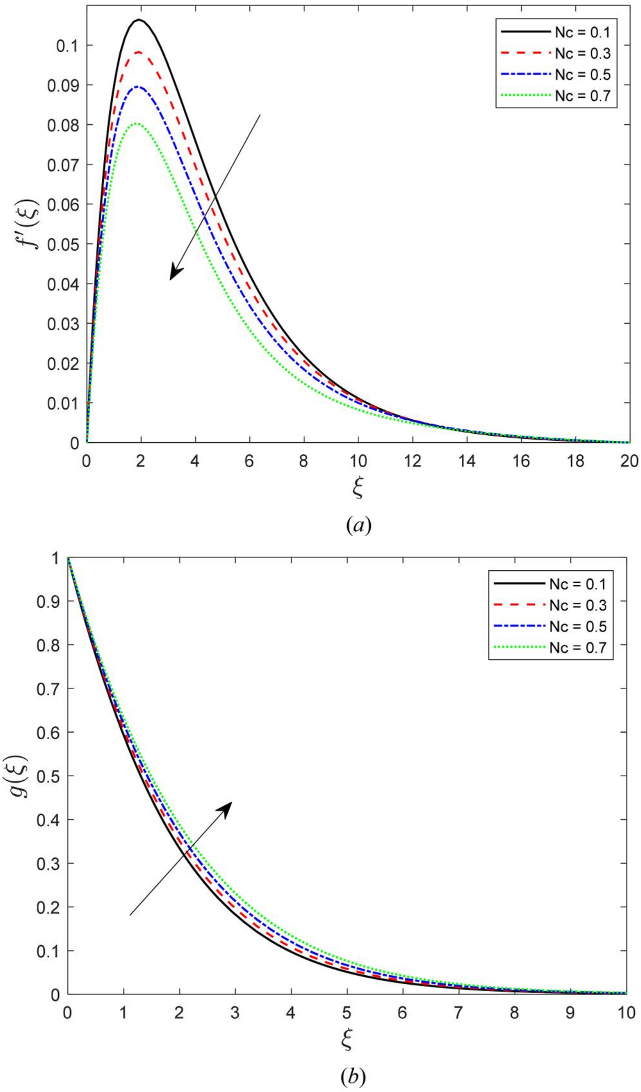

Figure 6. (*a*) Graphical illustration of Nc on $f'(\xi)$. (*b*) Graphical illustration of Nc on $g(\xi)$.

induces temperature fluctuations because of the random motion of nanoparticles. These fluctuations contribute to local variations in temperature within the fluid, impacting the thermal profile of the bio-convection Casson nanofluid. This enhancement influences the temperature distribution, potentially leading to improved heat transfer characteristics.

4.7. Behavior of mixed convection parameter

The important role of mixed convection parameter is characterizing the relative strengths of both the free and forced convection. It refers to the combined influence of natural and force convection. In general, the natural convection is driven by the buoyancy force and the forced convection is induced by an external source. Figures 8*a*, *b* illustrates the significance of the mixed convection parameter on the profiles of axial and transverse velocity distribution. The flow pattern of the axial velocity is affected by the interaction between buoyancy and inertial force. To present the description of the concerned parameter the range of this factor is restricted to 0.5–1.1. The

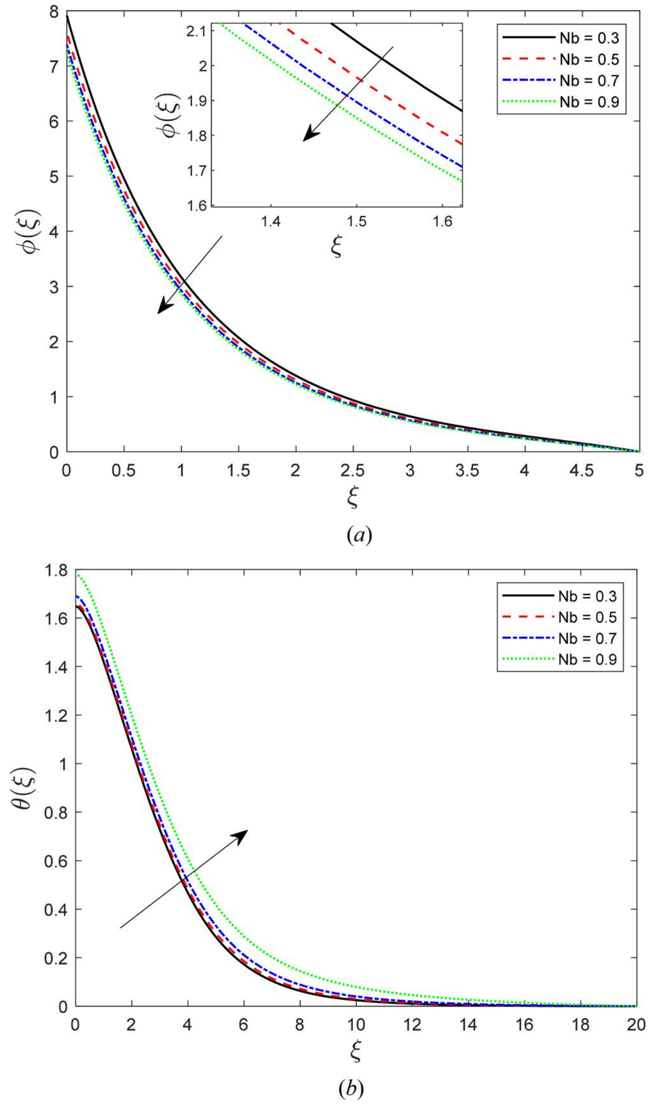

Figure 7. (*a*) Graphical illustration of Nb on $\phi(\xi)$. (*b*) Graphical illustration of Nb on $\theta(\xi)$.

enhanced mixed convection surprisingly augments the axial velocity distribution. The fact is, for the higher mixed convection, forced convection dominate over the natural convection, resulting a more uniform velocity profile. Further, the transverse velocity profile deployed a reverse effect to suppress the development of boundary layer for the higher mixed convection parameter.

4.8. Effect of thermophoresis parameter

Figure 9 portrays the characteristic of the thermophoresis factor on the temperature distribution of the Casson nanofluid. The description of the proposed factor on the temperature profile depends upon several key factors. The nondimensional parameter refers to the motion of the particles in response to the temperature gradient. It represents the strength of this effect and it influences the nanoparticles move in a fluid subjected to a temperature difference. It is a phenomenon

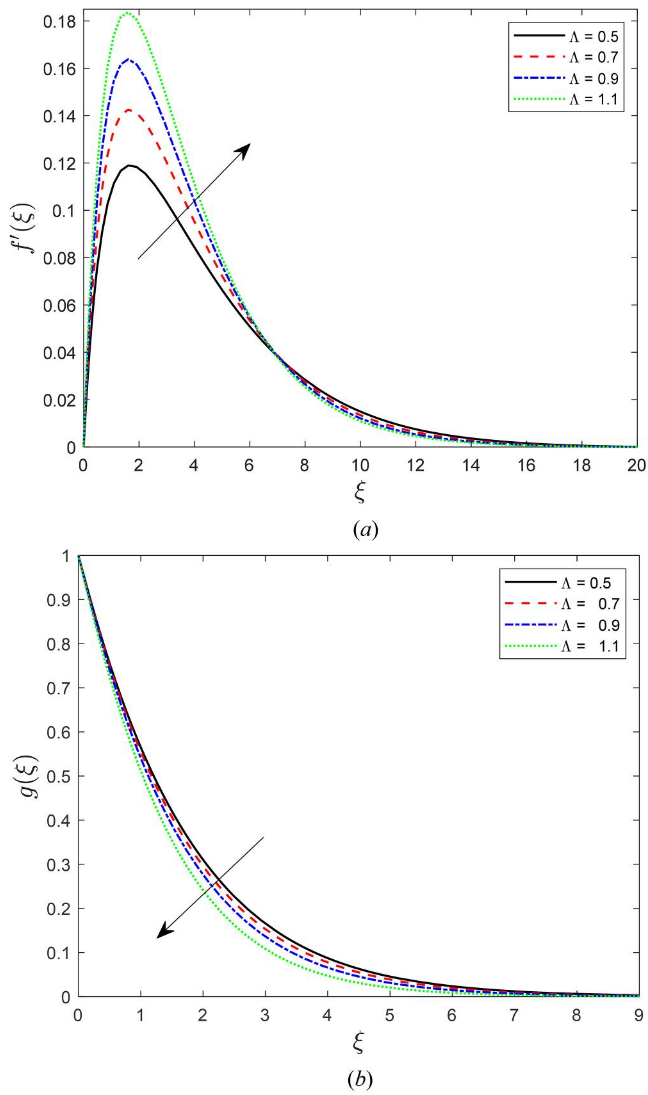

Figure 8. (*a*) Graphical illustration of Λ on $f'(\xi)$. (*b*) Graphical illustration of Λ on $g(\xi)$.

where the motion of fluid is biological factors i.e. the presence of microorganism. Further, the Casson fluid is a non-Newtonian fluid model that accounts for the yield stress of certain materials. A higher thermophoresis parameter leads to enhance the motion of nanoparticles with respect to temperature gradient. The yield stress produces due to the Casson fluid model that means the fluid will not start until a certain stress is applied. The thermophoresis parameter will influence the yield stress.

4.9. Effect of thermal radiation and Eckert number

Figures 10 and 11 exhibit the effect of radiating heat effect for the nitration of thermal radiation and the Eckert number on the Casson fluid temperature distribution. The factor thermal radiation is described as the emission of electromagnetic waves because of the temperature of the object. The inclusion of the thermal radiation significantly affects the temperature profile. However, the

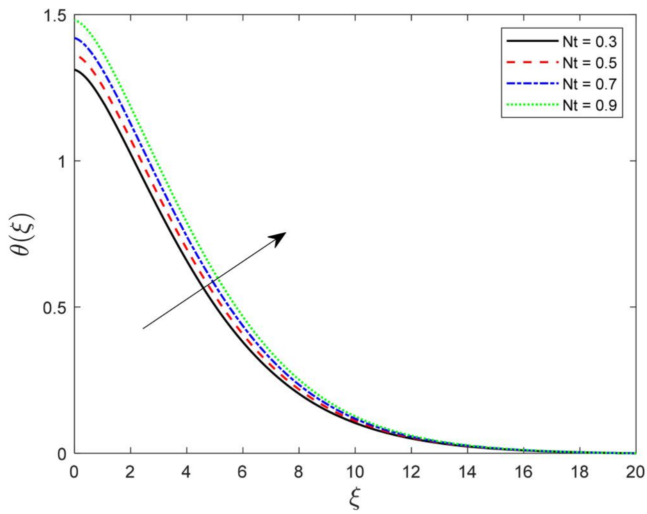

Figure 9. Graphical illustration of Nt on $\theta(\xi)$.

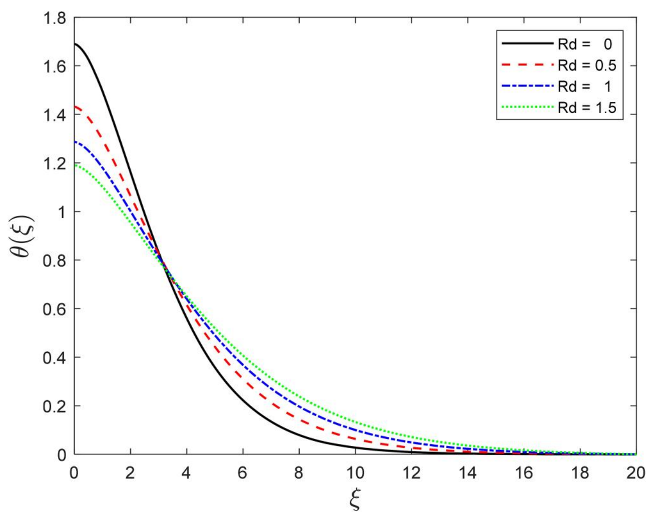

Figure 10. Graphical illustration of Rd on $\theta(\xi)$.

increased thermal radiation enhances heat transfer within the fluid. Radiative heat transfer supposed to more pronounce at higher temperature enriches the temperature profile. The dimensionless parameter Eckert number described as the ratio of the kinetic energy with respect to its enthalpy. In a bio-convection Casson nanofluid, Ec exhibits the balance between the kinetic energy and enthalpy. Changes in Ec also affect the temperature profile by influencing the heat absorbed during fluid flow. The efficient heat transfer is obtained that enhances the temperature distribution is due to the dominance of the enthalpy over the kinetic energy.

4.10. Behavior of the buoyancy ratio parameter

The factor buoyancy ratio is obtained due to the relationship between the solutal and thermal buoyancy parameter exhibiting their ratio. Figure 12 projects the limitations of the buoyancy ratio parameter on the fluid temperature of the non-Newtonian fluid. The characteristic of the

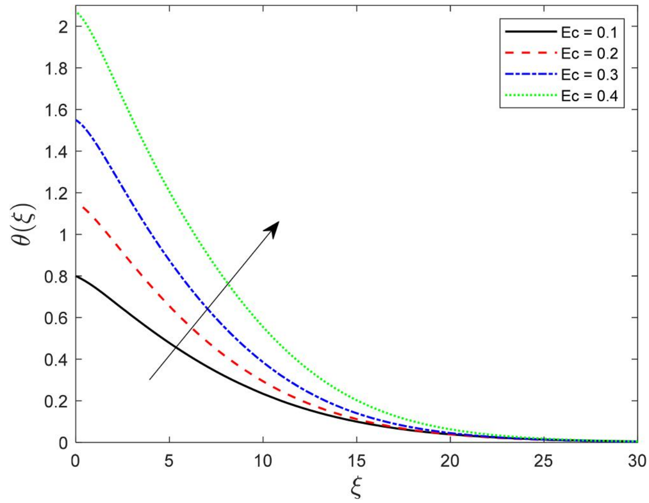

Figure 11. Graphical illustration of Ec on $\theta(\xi)$.

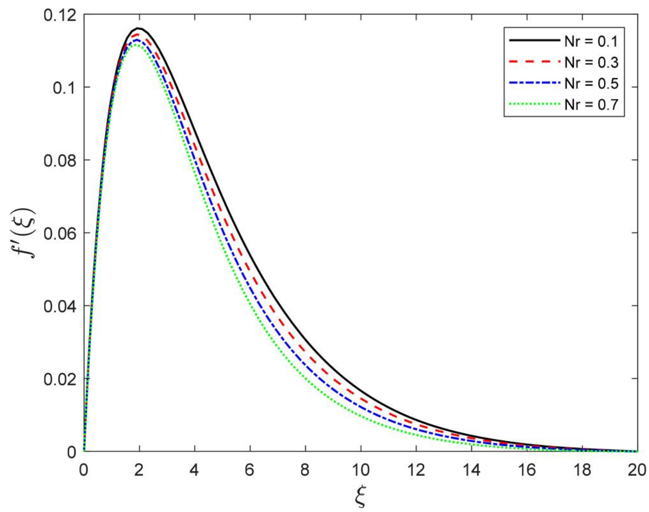

Figure 12. Graphical illustration of Nr on $f'(\xi)$.

proposed factor is exhibited within the standard range of $0.1 \leq Nr \leq 0.7$. It has a crucial role in retarding the temperature profile due to the heating of the surface. The buoyancy forces associated to the density differences among the fluid layers, while the viscous force is related to the resistance of the fluid to shear deformation. However, an increase in the buoyancy ration due to the heating of the surface significantly attenuates the temperature of the fluid. This leads to retards the heat transmission characteristics as the fluid experiences a decreased circulation. One of the interesting facts is that the interaction between the bio-convection and Casson fluid combined with buoyancy ratio resulting a nonlinear behavior which favors in retardation in the fluid temperature.

4.11. Effect of chemical reaction parameter

Figure 13 exhibits the significant characteristic of the chemical reaction parameter on the profile of fluid concentration. The factor, reaction rate is the rate at which the chemical reaction occurs

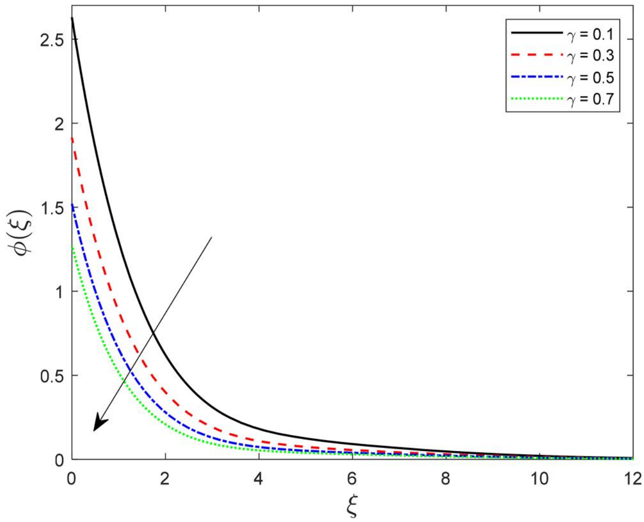

Figure 13. Graphical illustration of γ on $\phi(\xi)$.

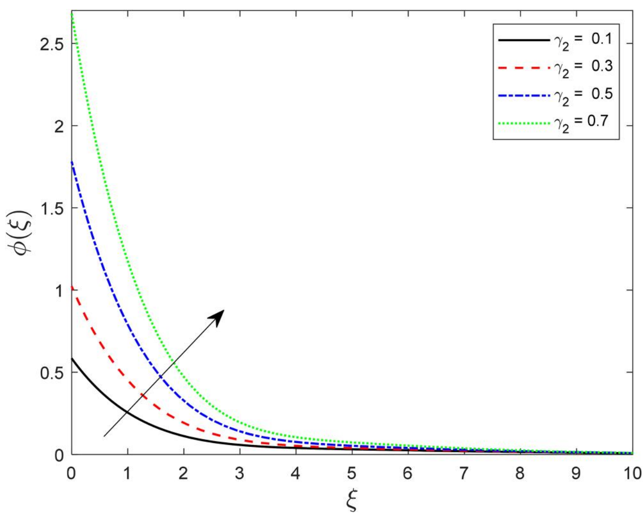

Figure 14. Graphical illustration of γ_2 on $\phi(\xi)$.

provides significant contribution on the profiles. Higher concentration lead to faster depletion produces less concentration within the distribution. Here, the type of species involved will determine the nature of the concentration. The change in concentration is also affected by the Brownian as well as the thermophoresis parameter. Therefore, the higher concentration obtained due to increasing chemical reaction attenuates the solutal bounding surface thickness throughout.

4.12. Effect of solutal biot number and microorganism difference parameter

The convective concentration boundary condition leads to show the existence of the solutal Biot number in the transformed form. Figures 14 and 15 show the experience of the solutal Biot number along with microorganisms' difference parameter on the fluid concentration profile. The ratio between the solute diffusion rate and the rate bio-convection is depicted the role of solutal Biot number. The numerical values considered for the description describes the behavior of the solute

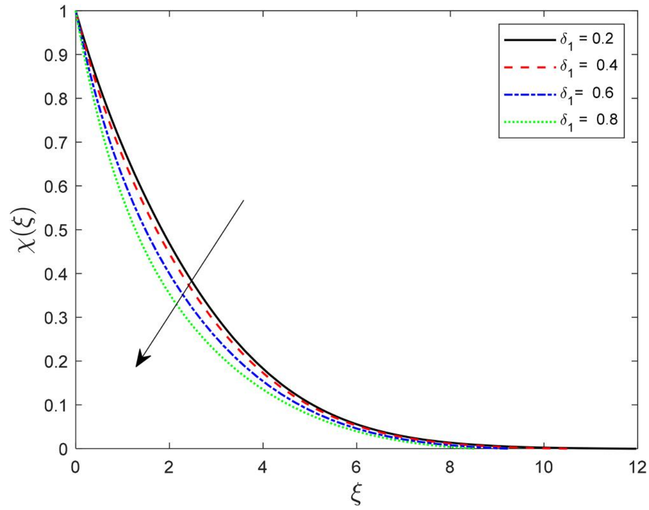

Figure 15. Graphical illustration δ_1 on $\chi(\xi)$.

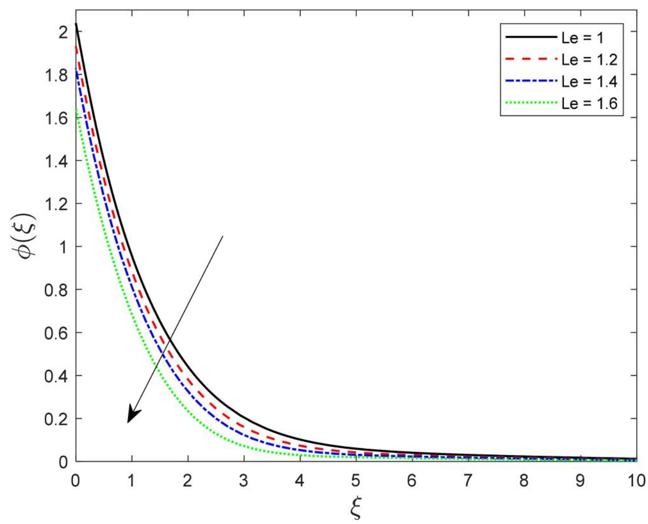

Figure 16. Graphical illustration of Le on $\phi(\xi)$.

diffusion rate to the bio-convection rate. For the high solutal Biot number, the solute diffusion rate is faster than that of bio-convection rate. Therefore, the concentration profile of the solute is pronounced highly within the nanofluid, as diffusion dominates the transport processes. However, microorganism difference reflects the difference in the characteristics of the microorganisms in the fluid, including the factors such as swimming sped, chemotactic sensitivity, etc. microorganism with different characteristics induce complex fluid motion which retards the profile for its higher values.

4.13. Effect of Lewis numbers

The flow of bio-convection Casson fluid characterized by Lewis number (Le) and bio-convection Lewis number (Le) due to the occurrence of the solutal diffusion and bio-convection diffusions.

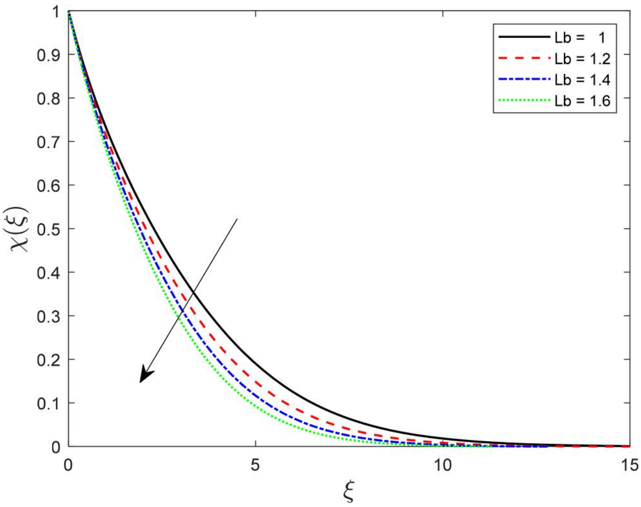

Figure 17. Graphical illustration of Lb on $\chi(\xi)$.

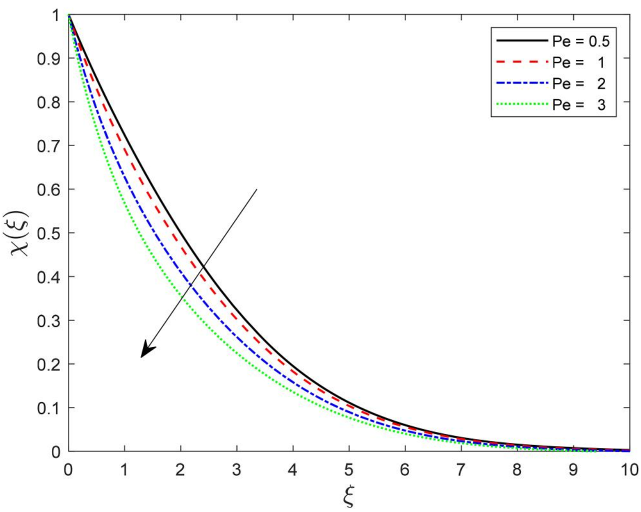

Figure 18. Graphical illustration of Pe on $\chi(\xi)$.

Figures 16 and 17 illustrates the role of (Le) on the concentration profile and (Lb) on the bio-convection profiles respectively. The relationship between the thermal and solutal diffusion in a fluid describes the dimensionless number, Le. However, the variation presents that, higher Lewis number implies, thermal diffusion is greater dominant than solutal diffusion. This lead to a significant deceleration in the fluid concentration distribution. Further, the behavior for the less Lewis number is accordingly varies within the flow domain. In the case of biological convection, the parameter (Lb) arises. A higher (Lb) indicates that the biological activity has a stronger retardation on the ass transport phenomenon compared to others and this significantly reduces the bio-concoction profile.

4.14. Effect of Peclet number

Figure 18 displays the impact of Peclet number on the bio-convection microorganism profiles. The relative importance of the convection to diffusion is presented by the nondimensional parameter by *Pe*. In the case of bio-convection Casson nanofluid, the Peclet number influences the dominance of nanofluid which retards the profile significantly.

5. Conclusions

The bioconvective nanofluid flow with motile microorganisms over a rotating disk is analyzed in the present article. The impact of dissipative heat combined with Brownian motion and thermophoresis energies the flow properties. However, Numerical simulation for the various flow profiles is obtained employing the traditional Runge kutta fourth-order technique. The characteristics of pertinent parameters involved in the flow phenomena are obtained and described briefly. Further, the outstanding outcomes are deployed below:

- The simulated values of the heat and solutal transfer rate conforms a good correlation with the earlier study that leads to validation as well as convergence criteria of the proposed methodology.
- The resistivity offered by the implementation of magnetic property along with porosity attenuates the axial and transverse velocity, however the impact is reversed in case of fluid temperature.
- The non-Newtonian factor, Casson parameter also favors in reducing the velocity profile significantly.
- The mixed convection due to the interaction of both the buoyant forces retards the axial velocity but it augments the transverse velocity further the bio convection parameter shows opposite impact.
- The coupling constant for the impact of dissipation and radiating heat due to thermal radiation boots up the fluid temperature.

Disclosure statement

No potential conflict of interest was reported by the author(s).

ORCID

S. R. Mishra http://orcid.org/0000-0002-3018-394X
Titilayo M. Agbaje http://orcid.org/0000-0002-8813-0955
Rupa Baithalu http://orcid.org/0000-0003-0672-0140
Subhajit Panda http://orcid.org/0000-0002-4865-0657

References

[1] Y. Li, A. Majeed, N. Ijaz, K. Barghout, M. R. Ali and T. Muhammad, "Melting thermal transportation in bioconvection Casson nanofluid flow over a nonlinear surface with motile microorganism: application in Bioprocessing Thermal Engineering," *Case Stud. Thermal Eng.*, vol. 49, pp. 103285, 2023. DOI: 10.1016/j.csite.2023.103285.

[2] P. Raut and S. R. Mishra, "Diversified impact of carbon nanotubes on the flow of micropolar nanofluid over a permeable expanding/contracting surface with thermal radiation," *Mod. Phys. Lett. B*, vol. 38, no. 08, pp. 2450049, 2023. DOI: 10.1142/S0217984924500490.

[3] M. H. Shahzad, A. U. Awan, K. Guedri, B. M. Fadhl and M. Oreijah, "Entropy-based investigation of blood flow in elliptical multi-stenotic artery with hybrid nanofluid in a fuzzy environment: applications as drug carriers for Brain Diseases," *Eng. Appl. Artif. Intell.*, vol. 130, pp. 107695, 2024. DOI: 10.1016/j.engappai.2023.107695.

[4] H. Waqas, S. Ali Khan and T. Muhammad, “Thermal analysis of magnetized flow of AA7072-AA7075/blood-based hybrid nanofluids in a rotating channel,” *Alexandria Eng. J.*, vol. 61, no. 4, pp. 3059–3068, 2022. DOI: 10.1016/j.aej.2021.08.033.

[5] W. Shao, *et al.*, “Statistical approach on optimizing heat transfer rate for au/Fe_3O_4-blood nanofluid flow with entropy analysis used in drug delivery system,” *Case Stud. Thermal Eng.*, vol. 54, pp. 104008, 2024. DOI: 10.1016/j.csite.2024.104008.

[6] S. Panda, T. Thumma, S. Ontela, S. R. Mishra and P. K. Pattnaik, “A numerical study on model-based comparative analysis for MHD magnetite (Fe_3O_4) and cobalt ferrite ($CoFe_2O_4$) flow past a heated shrinking Riga surface with radiative heat flux,” *J. Magn. Magn. Mater.*, vol. 586, pp. 171212, 2023. DOI: 10.1016/j.jmmm.2023.171212.

[7] S. Panda, G. Pradhan, D. Nayak, P. K. Pattnaik and S. R. Mishra, “Presentation of entropy due to heat transfer irreversibility of MHD Williamson fluid over an inclined channel,” *Mod. Phys. Lett. B*, vol. 38, no. 07, pp. 2450010, 2023. DOI: 10.1142/S0217984924500106.

[8] R. Baithalu, S. R. Mishra, P. K. Pattnaik and S. Panda, “Optimizing shear and couple stress analysis for the magneto-micropolar dissipative nanofluid flow toward an elongating surface: a comprehensive RSM-ANOVA investigation,” *J Therm Anal Calorim*, vol. 149, no. 4, pp. 1697–1713, 2023. DOI: 10.1007/s10973-023-12741-w.

[9] S. Tinker, S. R. Mishra, P. K. Pattnaik and R. P. Sharma, “Simulation of time-dependent radiative heat motion over a stretching/shrinking sheet of hybrid Nanofluid: stability analysis for dual solutions,” *Proc. Inst. Mech. Eng. Part N: J. Nanomater. Nanoeng. Nanosyst.*, vol. 236, no. 1–2, pp. 19–30, 2022. DOI: 10.1177/23977914211069021.

[10] R. Baithalu and S. R. Mishra, “On the free convection of Magneto-micropolar fluid in association with thermal radiation and chemical reaction and optimized heat transfer rate using response surface methodology,” *Mod. Phys. Lett. B*, vol. 37, no. 33, pp. 2350171, 2023. DOI: 10.1142/S0217984923501713.

[11] R. Baithalu, S. R. Mishra and N. Ali Shah, “Sensitivity analysis of various factors on the micropolar hybrid nanofluid flow with optimized heat transfer rate using response surface methodology: a statistical approach,” *Phys. Fluids*, vol. 35, no. 10, pp. 102016, 2023. DOI: 10.1063/5.0171265.

[12] P. K. Pattnaik, J. R. Pattnaik, S. R. Mishra and K. S. Nisar, “Variation of the shape of Fe_3O_4-nanoparticles on the heat transfer phenomenon with the inclusion of thermal radiation,” *J. Therm. Anal. Calorim.*, vol. 147, no. 3, pp. 2537–2548, 2021. DOI: 10.1007/s10973-021-10605-9.

[13] M. T. Akolade and Y. O. Tijani, “A comparative study of three dimensional flow of Casson–Williamson nanofluids past a Riga plate: spectral quasi-linearization approach,” *Partial Differ. Equ. Appl. Math.*, vol. 4, pp. 100108, 2021a. DOI: 10.1016/j.padiff.2021.100108.

[14] N. Acharya, “Spectral quasi linearization simulation of radiative nanofluidic transport over a bended surface considering the effects of multiple convective conditions,” *Eur. J. Mech. B/Fluids*, vol. 84, pp. 139–154, 2020. DOI: 10.1016/j.euromechflu.2020.06.004.

[15] M. O. Lawal, K. B. Kasali, H. A. Ogunseye, M. O. Oni, Y. O. Tijani and Y. T. Lawal, “On the mathematical model of Eyring–Powell nanofluid flow with non-linear radiation, variable thermal conductivity and viscosity,” *Partial Differ. Equ. Appl. Math.*, vol. 5, pp. 100318, 2022. DOI: 10.1016/j.padiff.2022.100318.

[16] A. Sahoo and R. Nandkeolyar, “Entropy generation in magnetohydrodynamic radiative non-Darcy slip flow of a Casson nanofluid with hall effects and activation energy,” *J. Magn. Magn. Mater.*, vol. 575, pp. 170712, 2023. DOI: 10.1016/j.jmmm.2023.170712.

[17] R. E. Bellman and R. E. Kalaba, *Quasilinearization and Nonlinear Boundary-Value Problems, Modern Analytic and Computational Methods in Science and Mathematics*, Elsevier; 1965.

[18] S. S. Motsa, “A new spectral local linearization method for nonlinear boundary layer flow problems,” *J. Appl. Math.*, vol. 2013, pp. 1–15, 2013. DOI: 10.1155/2013/423628.

[19] N. Acharya, “Magnetically driven MWCNT-Fe_3O_4-water hybrid nanofluidic transport through a micro-wavy channel: a novel MEMS design for drug delivery application,” *Mater. Today Commun.*, vol. 38, pp. 107844, 2024. DOI: 10.1016/j.mtcomm.2023.107844.

[20] N. Acharya, “Spectral simulation to investigate the effects of nanoparticle diameter and nanolayer on the ferrofluid flow over a slippery rotating disk in the presence of low oscillating magnetic field,” *Heat Transf.*, vol. 50, no. 6, pp. 5951–5981, 2021. DOI: 10.1002/htj.22157.

[21] N. Acharya, “Framing the impacts of highly oscillating magnetic field on the ferrofluid flow over a spinning disk considering nanoparticle diameter and solid–liquid interfacial layer,” *J. Heat Transf.*, vol. 142, no. 10, pp. 102503, 2020. DOI: 10.1115/1.4047503.

[22] N. Acharya, “Spectral quasi linearization simulation on the radiative nanofluid spraying over a permeable inclined spinning disk considering the existence of heat source/sink,” *Appl. Math. Comput.*, vol. 411, pp. 126547, 2021. DOI: 10.1016/j.amc.2021.126547.

[23] N. Acharya, “Spectral quasi linearization simulation on the hydrothermal behavior of hybrid nanofluid spraying on an inclined spinning disk,” *Partial Differ. Equ. Appl. Math.*, vol. 4, pp. 100094, 2021. DOI: 10.1016/j.padiff.2021.100094.
[24] S. A. Shehzad, *et al.*, “Numerical and regression analysis of horizontal magnetic field in slippery nanofluid flow with Arrhenius activation energy,” *J. Mol. Liq.*, vol. 392, pp. 123522, 2023. DOI: 10.1016/j.molliq.2023.123522.
[25] A. Rauf, M. Irfan, M. Omar, T. Mushtaq, S. A. Shehzad and M. N. Bashir, “Numerical study of micropolar nanofluid flow between two parallel permeable disks with thermophysical property and Arrhenius activation energy,” *Int. Commun. Heat Mass Transf.*, vol. 137, pp. 106272, 2022. DOI: 10.1016/j.icheatmasstransfer.2022.106272.
[26] U. Hani, J. A. Khan, A. Rauf, F. Mustafa and S. A. Shehzad, “Bayesian and Numerical Techniques for Non-Newtonian Bödewadt Nanofluid Flow Above a Stretchable Stationary Disk,” *Arab. J. Sci. Eng.*, vol. 47, no. 12, pp. 15931–15945, 2022. DOI: 10.1007/s13369-022-06773-x.
[27] T. Hayat, T. Muhammad, S. S. Shehzad and A. Alsaedi, “On magnetohydrodynamic flow of nanofluid due to a rotating disk with slip effect: a numerical study,” *Comput. Methods Appl. Mech. Eng.*, vol. 315, pp. 467–477, 2017. DOI: 10.1016/j.cma.2016.11.002.
[28] K. U. Rehman, M. Y. Malik, M. Zahri and M. Tahir, “Numerical analysis of MHD Casson Navier’s slip nanofluid flow yield by rigid rotating disk,” *Results Phys.*, vol. 8, pp. 744–751, 2018. DOI: 10.1016/j.rinp.2018.01.017.
[29] J. Ahmed, *et al.*, “Magneto-bioconvection flow of Casson nanofluid configured by a rotating disk in the presence of gyrotatic microorganisms and Joule heating,” *Heliyon*, vol. 9, no. 8, pp. e18028, 2023. DOI: 10.1016/j.heliyon.2023.e18028.